JGR Solid Earth

RESEARCH ARTICLE
10.1029/2020JB020293

A Tsunami Warning System Based on Offshore Bottom Pressure Gauges and Data Assimilation for Crete Island in the Eastern Mediterranean Basin

Yuchen Wang[1], Mohammad Heidarzadeh[2], Kenji Satake[1], Iyan E. Mulia[1], and Masaki Yamada[3]

[1]Earthquake Research Institute, The University of Tokyo, Tokyo, Japan, [2]Department of Civil and Environmental Engineering, Brunel University London, Uxbridge, UK, [3]Department of Geology, Faculty of Science, Shinshu University, Nagano, Japan

Key Points:
- A tsunami warning system is proposed for Crete Island, Greece, based on Offshore Bottom Pressure Gauges and data assimilation
- The designed system achieves a high accuracy in forecasting the arrival time and amplitude for tsunamis in the Eastern Mediterranean Basin
- The designed system successfully forecasts the recent real tsunami of the 2 May 2020 off Crete Island, Greece

Supporting Information:
- Supporting Information S1

Correspondence to:
Y. Wang,
ywang@eri.u-tokyo.ac.jp

Citation:
Wang, Y., Heidarzadeh, M., Satake, K., Mulia, I. E., & Yamada, M. (2020). A tsunami warning system based on offshore bottom pressure gauges and data assimilation for Crete Island in the Eastern Mediterranean Basin. *Journal of Geophysical Research: Solid Earth*, *125*, e2020JB020293. https://doi.org/10.1029/2020JB020293

Received 4 JUN 2020
Accepted 16 SEP 2020
Accepted article online 20 SEP 2020

Abstract The Eastern Mediterranean Basin (EMB) is under the threat of tsunami events triggered by various causes including earthquakes and landslides. We propose a deployment of Offshore Bottom Pressure Gauges (OBPGs) around Crete Island, which would enable tsunami early warning by data assimilation for disaster mitigation. Our OBPG network consists of 12 gauges distributed around Crete Island, with a 100-km interval, based on three criteria to select the locations. The station network must have a good azimuthal coverage and have enough (>50 km) distance from the coast, and the OBPGs are placed at the locations where the most energetic wave dynamics occur, which is confirmed by Empirical Orthogonal Function (EOF) analysis of pre-calculated tsunami scenarios. We demonstrate three test cases comprising a hypothetical seismogenic tsunami in east Sicily, a hypothetical landslide tsunami in the Aegean Sea, and the real tsunami event of the May 2020 off the Crete earthquake. Our designed OBPG network achieves an accuracy of 88.5% for the hypothetical seismogenic tsunami and 87.3% for the hypothetical landslide tsunami with regard to the forecasting of first tsunami peak. For the real event of May 2020, it predicts the tsunami arrival at tide gauge NOA-04 accurately; the observed and forecasted amplitudes of the first wave are 5.0 cm and 4.5 cm, respectively. The warning lead time for the May 2020 event was ~10 min. Therefore, our results reveal that the assimilation of OBPG data can satisfactorily forecast the amplitudes and arrival times for tsunamis in the EMB.

1. Introduction

Tsunamis in the Eastern Mediterranean Basin (EMB) have raised significant concern over the past years, in particular following the July 2017 Bodrum-Kos (Turkey-Greece) and the May 2020 off the Crete earthquakes and tsunamis (Figures 1 and 2) (Heidarzadeh et al., 2017; Papadopoulos et al., 2020; Yalciner et al., 2017). In the catalogue of tsunamis in the Mediterranean Sea, Soloviev (1990) identified numerous tsunami events in the Aegean Sea, Sea of Crete, and other locations in the EMB. The southern Greece, including Crete Island, the Cyclades, and the Dodecanese Islands, is among the most active regions in terms of seismicity. The main cause of tsunami generation in this region is tectonic activity associated with strong earthquakes (Papadopoulos, Daskalaki, & Fokaefs, 2007). For example, earthquakes often occur in the south-central Aegean Sea. The 1956 Amorgos earthquake (Mw 7.7–7.8) (Figure 1) was the largest one to strike Greece in the 20th century. The 1956 earthquake generated a strong tsunami that affected the northern shores of Crete Island. In Heraklion, the largest city in Crete, the 1956 tsunami arrived with a 2-m runup height and inundated 30 m inland. In Souda, a port city in the northwest of Crete Island, the measured tsunami runup height was 1.5 m (Okal et al., 2009). To the south of Crete Island, there is an active tsunamigenic zone of the Hellenic subduction zone (Figure 1) which has produced many large, shallow, and intermediate-depth earthquakes in the past (Papadopoulos, Daskalaki, Fokaefs, & Giraleas, 2007). For instance, the AD 365 earthquake (Mw 8.4) in the southwestern Crete Island was felt throughout the eastern Mediterranean Sea. Its tsunami inundated coastal sites in Africa, the Adriatic Sea, Greece, and Sicily and drowned thousands of people (Shaw et al., 2008). Moreover, the tsunamigenic zone in the east Aegean Sea also has a very high tsunami potential.

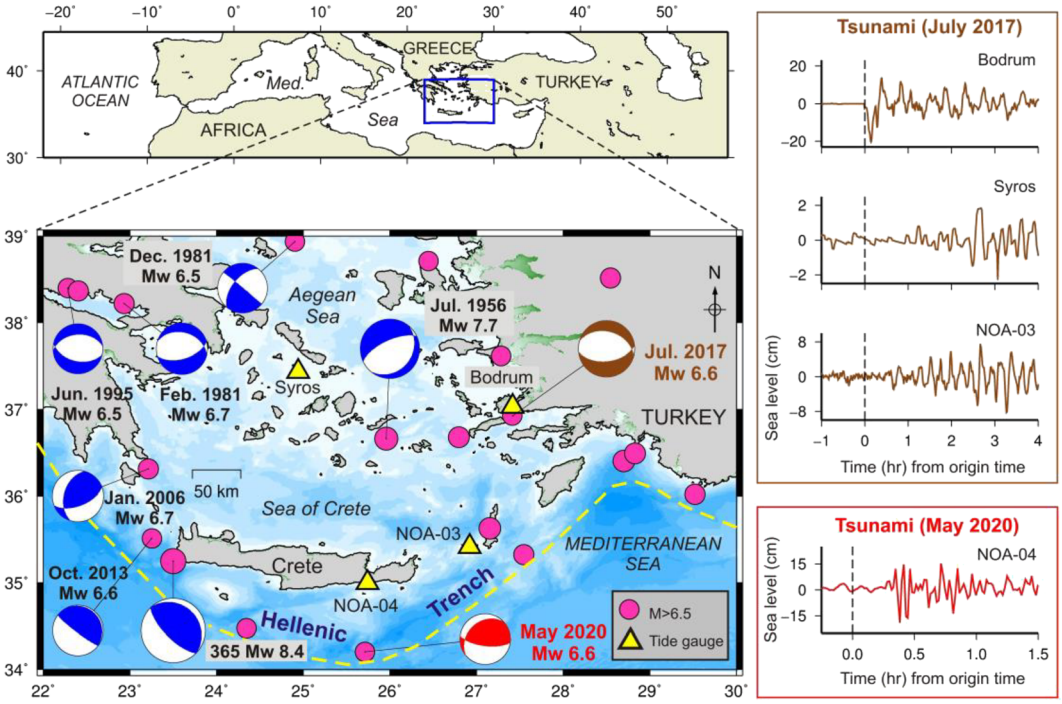

Figure 1. Location of Crete Island and the past earthquakes/tsunamis in the surrounding areas. The observed tsunami waveforms of the July 2017 Bodrum-Kos earthquake and the May 2020 off the Crete earthquake are plotted in the right panels. The focal mechanisms and magnitudes are based on USGS (the United States Geological Survey) earthquake catalogue.

The two recent events in the EMB region are the July 2017 Bodrum-Kos earthquake (Mw 6.6; Dogan et al., 2019; Yalciner et al., 2017) and the May 2020 off the Crete earthquake (Mw 6.6; The United States Geological Survey [USGS], 2020). The 2017 event occurred near the Turkey-Greece border and generated a moderate tsunami that caused damage in Bodrum Peninsula and in Kos (Heidarzadeh et al., 2017; Yalciner et al., 2017). The

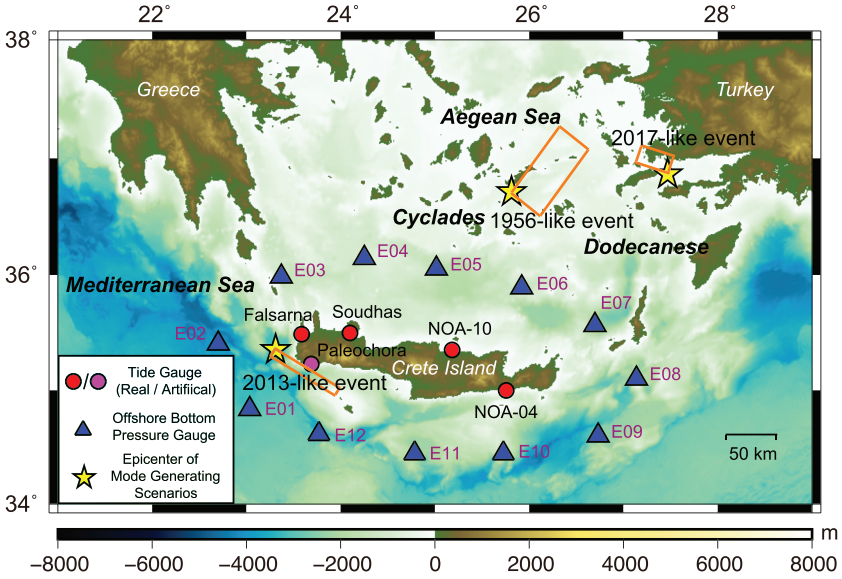

Figure 2. Locations of 12 designed Offshore Bottom Pressure Gauges (OBPGs) for the area around Crete Island in the Eastern Mediterranean Basin (blue triangles). Red circles are the real tide gauges on the island for waveform comparison. The pink circle is an artificial tide gauge considered in this study. Yellow stars indicate the epicenter of Mode Generating Scenarios (MGSs), and the orange rectangles indicate the locations and orientations of the faults.

tsunami was recorded by several tide gauges in the region (Figure 1) and caused some moderate damage with no casualties. The tsunami was also recorded by a tide gauge in the Kasos Island, approximately 30 km to the east of Crete (i.e., station NOA-03) (Figure 1). The May 2020 tsunami occurred south of Crete Island, following an Mw 6.6 earthquake. There were no reports of injuries or casualties in the aftermath of this event. The earthquake generated a tsunami that hit the southern coast of Crete Island at around 15–20 min after the earthquake and was recorded at tide gauge NOA-04 with amplitudes of 15–20 cm (Figure 1).

In addition to earthquakes, tsunamis in the EMB are also generated by landslides and volcanic eruptions (Samaras et al., 2015; Yalciner et al., 2014). Papadopoulos, Daskalaki, and Fokaefs (2007) studied 32 reliable cases of landslide tsunamis in the Mediterranean Sea. On 30 September 1650, a large tsunami occurred during the eruption of the submarine volcanic edifice Kolumbo in the Aegean Sea. It was generated by the submarine collapse of the volcanic cone (Dominey-Howes et al., 2000). The tsunami violently swept ships and fishing boats at Crete Island, and the wave overtopped the city's sea walls (Papadopoulos, Daskalaki, & Fokaefs, 2007). Yalciner et al. (2014) studied generation and propagation of landslide tsunamis in the EMB.

For disaster mitigation purposes, it is important to design an observational system aimed at tsunami early warning. Tsunami data assimilation, a recent technology for tsunami warning, relies on Offshore Bottom Pressure Gauges (OBPGs) which monitor the sea surface elevation and report the data in real time (Heidarzadeh & Gusman, 2018; Maeda et al., 2015; Satake, 2014). In the Nankai Trough offshore west Japan, a dense array of OBPGs known as DONET (the Dense Oceanfloor Network system for Earthquakes and Tsunamis) (Kaneda, 2010; Wang et al., 2018) has been deployed and is available for tsunami warning system. However, in the EMB such observational system is presently unavailable. In this study, we propose a potential tsunami early warning system for Crete Island based on the deployment of OBPGs. The system forecasts the tsunami by data assimilation approach. We demonstrate that our designed OBPG network is useful for forecasting both seismogenic and landslide tsunamis, by conducting experiments with two hypothetical tsunamis and the real tsunami of 2 May 2020.

2. Data and Method

2.1. Criteria for Optimal Location of the OBPGs

The tsunami early warning system based on OBPGs should be able to detect the tsunami signals efficiently and forecast the tsunami waveforms in a timely manner. In this study, three criteria are followed to design the optimal location of the OBPGs:

i. The network should have a large azimuthal coverage.
ii. The OBPGs should be located at appropriate distance from the coast.
iii. The OBPGs should be placed at the locations where the energetic dynamics occur.

We note that there might be some OBPGs that cannot meet the three criteria simultaneously, but we make sure that most OBPGs can satisfy these requirements. The tsunami early warning network needs to cover a large azimuthal coverage of the island, so that it can detect the tsunami signals from all directions. In this study, the design of OBPG locations is under the constraint that they surround the island with approximately 100 km interval. Moreover, in order to allow enough lead time for issuing warnings before the tsunami arrives at the coast, we also consider that the OBPGs are distanced at least 50 km from the coast.

In addition to these two criteria, the OBPGs should be placed at the locations where the energetic dynamics occur. To confirm the requirement of the third criterion, we apply Empirical Orthogonal Function (EOF) analysis. EOF is commonly used to decompose the data into spatial and temporal modes in earth science (Liu et al., 2018; Lorentz, 1956). The EOF spatial modes provide information about the areas where the modal activity is the highest, which correspond to the main energy distribution of a system (Cohen et al., 2003).

Assuming that there are n locations (grid points), and each location has a time series of length p, we create an $n \times p$ matrix $\boldsymbol{Z}$ that stores these data. The ith column of such a matrix contains the time series at the ith location (grid), while the jth row represents a snapshot of the whole region at the jth time step (Mulia et al., 2017; Navarrete et al., 2020). After removing the mean of each time series, the covariance matrix is formed by $\boldsymbol{R} = \boldsymbol{Z}^T\boldsymbol{Z}$. Then we solve the eigenvalue problem as formulated below:

Table 1
Parameters of Three Mode Generating Scenarios (MGSs) Used in This Study for Our EOF Analysis

Scenario number	Lon (°E)	Lat (°N)	Depth (km)	Strike (°)	Dip (°)	Rake (°)	Length (km)	Width (km)	Slip (m)
1 (2013-like event)	35.50	23.28	60.0	127	83	88	90.0	40.0	7.0
2 (1956-like event)	36.72	25.76	25.0	39	25	246	81.0	41.0	7.0
3 (2017-like event)	36.93	27.41	7.0	285	39	−73	25.0	15.0	8.0

$$\boldsymbol{RC} = \boldsymbol{C\Lambda} \tag{1}$$

where $\boldsymbol{C}$ is the matrix of eigenvectors $\boldsymbol{c}_i$ and $\boldsymbol{\Lambda}$ is a diagonal matrix containing the eigenvalues $\boldsymbol{\lambda}_i$. Each eigenvector presents a spatial mode, and the first EOF spatial mode is associated with the largest eigenvalue.

In our study, we select the region around Crete Island, within the geographical domain of 33–36°N, 22–28°E. We select the grids with a water depth of more than 300 m that cover the region of designed OBPGs. To perform the EOF analysis, we consider three tsunami scenarios which are called Mode Generating Scenarios (MGSs). The sources of the MGSs are adopted from the past real tsunami events in the EMB region, from west to east: the 2013 Platanos earthquake, the 1956 Amorgos earthquake, and the 2017 Bodrum-Kos earthquake (Figures 1 and 2). We adopt the same parameters of fault locations and focal mechanisms (Table 1) but amplify the slip values of each scenario (Table 1; last column) when computing the MGSs, in order to make the tsunami amplitude more evident in the EOF analysis area. The simulation of tsunami propagation and generation of three MGSs is described in section 2.2. After performing the EOF analysis, we check whether our designed OBPGs are placed at locations with large absolute EOF values.

2.2. Simulation of Seismogenic Tsunamis

We adopt the analytical dislocation model of Okada (1985) to compute the seafloor deformation for seismogenic tsunamis. The sea surface displacement is assumed to be the same as the seafloor deformation and is used as the initial condition for tsunami simulation according to the common practice in tsunami science (e.g., Satake, 2015). Then, we apply a linear long-wave model to simulate tsunami propagation, using the simulation package *JAGURS* (Baba et al., 2015; Satake, 1995; Satake & Heidarzadeh, 2017). Tsunami computation is performed on the supercomputer of Earthquake Information Center, The University of Tokyo. For computing the tsunamis arising from our three MGSs, the simulation time is 60 min since the earthquake origin time, and the spatial variation of water surface is stored every 10 s, resulting in 360 snapshots.

The bathymetry and topography dataset are derived from the General Bathymetric Chart of the Ocean released in 2014 (GEBCO_2014; Weatherall et al., 2015). We use a grid size of 30 arc sec (equivalent to ~925 m), and a time step of 1 s to satisfy the stability condition of Finite Difference Method. The simulated tsunami waveforms at the locations of the proposed OBPGs are used for data assimilation retrospectively. The waveforms recorded at tide gauges are employed for waveform comparison in order to examine the performance of our method. Four real and one artificial tide gauges around Crete Island are selected (Figure 2) which are as follows: NOA-04, NOA-10, Soudhas, Paleochora, and Falasarna. The stations of NOA-04 and NOA-10 are operated by the National Observatory of Athens (NOA). The station Soudhas belongs to the Permanent Service for Mean Sea Level (PSMSL). The station Paleochora serves as an Inexpensive Device for Sea Level Measurement (IDSL), which is developed by the Joint Research Centre (JRC) of the European Commission. The station Falasarna is a virtual tide gauge, intended to evaluate the tsunami hazards of the west Crete Island in our study.

2.3. Simulation of Landslide Tsunamis

To assess the tsunami hazards in the EMB thoroughly, we also consider tsunamis triggered by landslides. We use a two-layer hydrodynamic model to simulate the generation and propagation of landslide tsunamis (Maeno & Imamura, 2011; Ren et al., 2020).

Here we assume that a submarine landslide occurs in the Cyclades region. We focus on a smaller region of 36.5–37.5°N, 25.0–26.0°E, and resample the GEBCO_2014 grid to a finer resolution of 6 arc sec. The time step is 0.1 s for modeling the generation phase of landslide tsunami. In our two-layer model, the slides are simulated as the bottom layer whose motion is fully coupled to that of the surrounding water. The submarine

landslide layer is of arbitrary geometry and is represented as a dense Newtonian fluid. Additional information about landslide modeling process and associated hydrodynamic equations are given in Kawamata et al. (2005) and Ren et al. (2020). We simulate the landslide and the triggered tsunami for the first 5 min (i.e., the generation phase). Then, we continue the computation of the tsunami propagation in a larger region of 34.0–38.0°N, 24.0–28.0°E, with a resolution grid of 6 arc sec, and a time step of 0.25 s, using the two-layer/*JAGURS* models. In the two layer-model, the surface elevation and the horizontal velocities at the end of landslide generation phase are used as the initial condition, while only the surface elevation was used in *JAGURS* model for tsunami propagation (Heidarzadeh et al., 2014; Satake, 2012). Comparison of these two models is shown in Supporting Information S1, which shows that they are similar. This might indicate the horizontal velocity at the end of landslide generation phase is negligible for tsunami propagation modeling. In our experiment of the hypothetical landslide tsunamis, we adopted the results of the two-layer model.

2.4. Tsunami Data Assimilation

Tsunami data assimilation is a tsunami early warning approach which does not require information about initial condition but is directly applied to sea surface elevation data during tsunami propagation for forecast (Gusman et al., 2016; Maeda et al., 2015). It successively assimilates the real-time offshore sea surface observation and estimates the regional tsunami status. Wang, Satake, et al. (2019) applied this approach to the 2015 Torishima volcanic tsunami earthquake retrospectively and successfully forecasted the tsunami height and arrival time based only on offshore sea surface observations. Recently, this approach is also taken into consideration when designing the offshore observational devices. For example, Heidarzadeh et al. (2019) proposed a potential deployment of OBPGs in the western Mediterranean Sea. Navarrete et al. (2020) designed a network of tsunameters off the Chilean coast based on tsunami data assimilation.

The tsunami status at nth time step is represented as: $\boldsymbol{x_n}(h(n\Delta t, x, y), M(n\Delta t, x, y), N(n\Delta t, x, y))$, where h is the sea surface height, M and N are horizontal flow fluxes in the x and y directions, respectively, and Δt is the time step for numerical simulations. Assuming that the total grid number is L and the number of OBPGs is m, the tsunami status vector $\boldsymbol{x_n}$ will be a $3L \times 1$ column vector. M and N are defined as $M = u(d + h)$ and $M = v(d + h)$ where u and v are horizontal velocities in the x and y directions, respectively, and d is water depth. The tsunami status is forecasted by multiplying the tsunami status of last time step with a propagation matrix $\boldsymbol{F}$ $(3L \times 3L)$, which is built from the tsunami propagation model (Equation 2). Here the superscripts f and a refer to forecasted (before correction) and assimilated (after correction) tsunami status, respectively.

$$\boldsymbol{x}_n^f = \boldsymbol{F}\boldsymbol{x}_{n-1}^a \tag{2}$$

$$\boldsymbol{x}_n^a = \boldsymbol{x}_n^f + \boldsymbol{W}\left(\boldsymbol{y}_n - \boldsymbol{H}\boldsymbol{x}_n^f\right) \tag{3}$$

where matrix $\boldsymbol{H}$ $(m \times 3L)$ is a sparse matrix that extracts the forecasted tsunami height of the corresponding stations, matrix $\boldsymbol{W}$ $(3L \times m)$ is a weight matrix for smoothing which is used to bring the forecasted tsunami status closer to the real wavefield, and $\boldsymbol{y}_n$ is real tsunami observation data that is obtained from the OBPGs. More details about the weight matrix $\boldsymbol{W}$ are described in Maeda et al. (2015). In Equation 3, the forecasted tsunami status (i.e., $\boldsymbol{x}_n^f$) is corrected by observation. The offshore OBPGs provide the data of tsunami height (h); then, tsunami flow velocities (u and v) are reconstructed during the assimilation process. After correction, we obtain the assimilated tsunami status $\boldsymbol{x}_n^a$, and it will be used for further forecasting in the next time step. During the assimilation process, Equations 2 and 3 are iterated repeatedly at each time step. Therefore, we are able to forecast the tsunami status based on the observation of OBPGs. In order to improve the efficiency of data assimilation, we adopt the technique of Green's Function-based Tsunami Data Assimilation (GFTDA; Furumura et al., 2018; Wang et al., 2017). We calculate the Green's functions between the proposed OBPGs and the tide gauges (Figures 3a–3c), and we use them to synthesize the forecasted tsunami waveforms during the assimilation process.

3. Application and Results

3.1. OBPG Locations and EOF Results

A total number of 12 OBPGs are selected for the observational network. They are located around Crete Island with an approximately 100 km interval and cover all directions (Figures 3 and 4). They are also

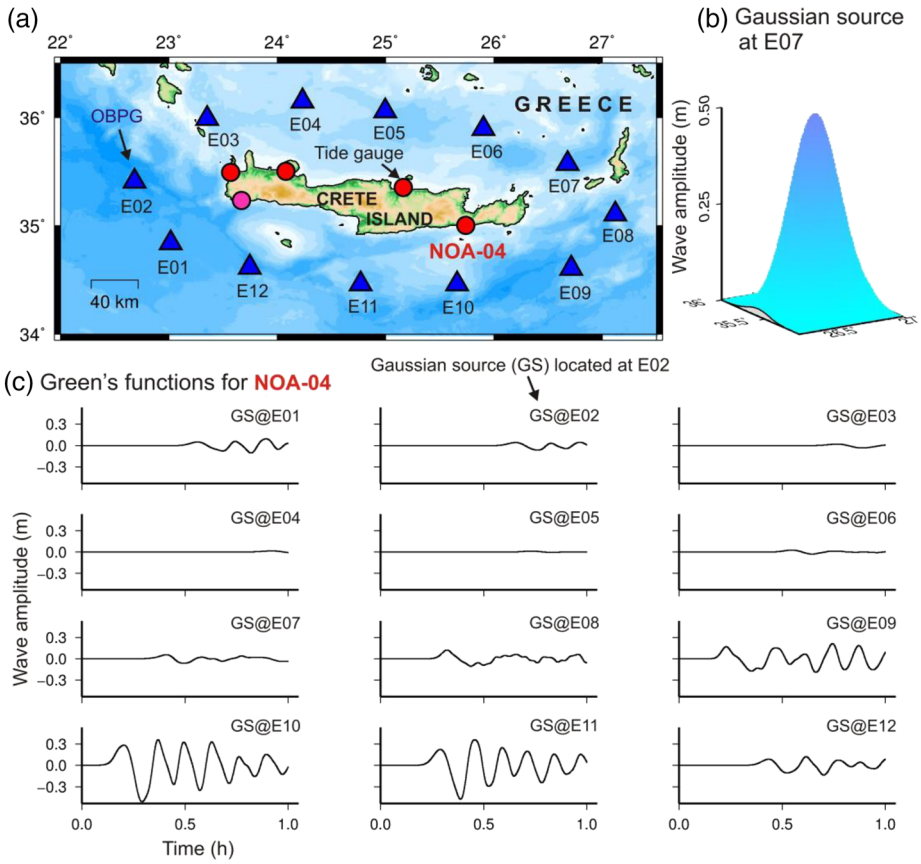

Figure 3. Green's Function-based Tsunami Data Assimilation (GFTDA). (a) The Green's function is defined as the waveform of tsunami propagation from an OBPG to a tide gauge (Wang et al., 2017). (b) The initial Gaussian-shaped source located at the OBPG station of E07 for calculating Green's functions. The characteristic distance of the Gaussian shape is 20 km (Maeda et al., 2015; Wang, Satake, et al., 2019). (c) The Green's functions for tide gauge NOA-04. There are 12 Green's functions that are resulted from each OBPG.

located at least 50 km from the coast to allow enough lead time for tsunami early warning. The first EOF spatial modes for three MGSs are plotted in Figure 4. For each EOF mode, there is a value of variance which represents its contribution to the total energy (Lorentz, 1956). For the three MGSs, that is, the 2013-like event, the 1956-like event, and the 2017-like event, the variances of the first EOF mode are 36.8%, 51.1%, and 41.2%, respectively. Since the variance of the first EOF mode is considerably larger than that of subsequent EOF modes (e.g., the second and third modes), using only the first EOF mode is sufficient to quantify the total energy of the tsunami dynamics in deep water (Mulia et al., 2019). It can be seen that most OBPGs are located at the areas with a large absolute EOF value for at least one MGS (Figures 4a–4c). For stations E06 and E07, they appear in the areas with large absolute values in both MGS1 and MGS2. The station E05 is located in the energetic regions of both MGS1 and MGS3. We note that the EOF energy is not maximum at the locations of E08, E09, and E10. However, EOF analysis is not the only criterion for designing the locations of OBPGs as discussed in section 2.1. The criteria of azimuthal coverage and distance to coast are other two criteria.

We note that the OBPG network is designed for providing warning to Crete Island as a pilot location. Therefore, in case the target of the warning system is another coastal location or a combination of locations, the same criteria can be applied to design an optimal OBPG network for those cases.

3.2. Early Warning for Hypothetical Seismogenic Tsunamis

Our first test of data assimilation is for a relatively far-field tsunami originating from the east Sicily, at the distance of approximately 900 km from Crete Island. The hypothetical earthquake (Mw 7.9) in east Sicily has a fault with a dimension of 95.0 km × 45.0 km, and its epicenter is located at 37.266°N, 15.686°E. The depth is

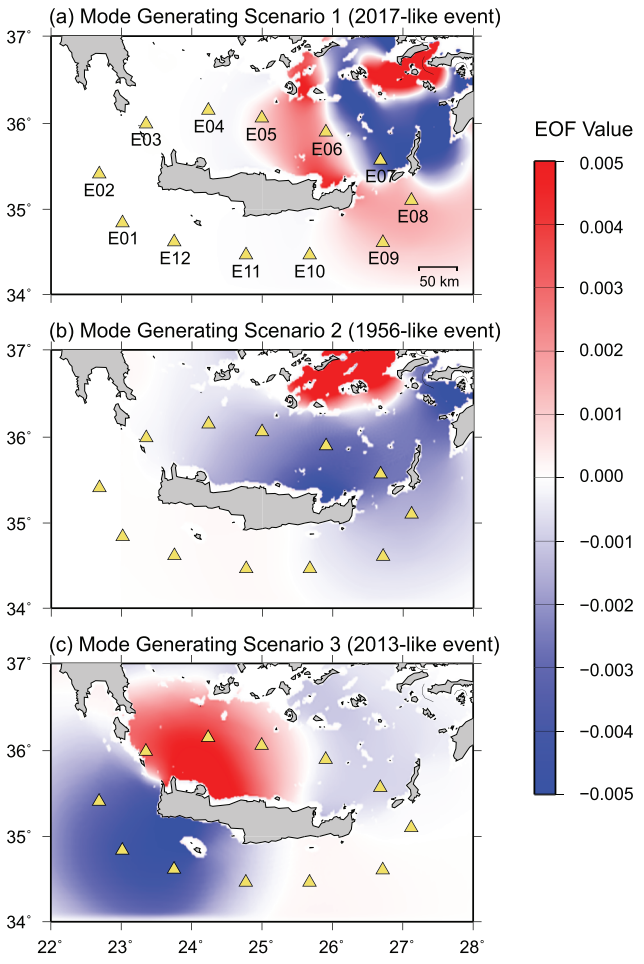

Figure 4. The first EOF spatial mode of three MGSs which are used for confirming the selection of the OBPG locations. Most of OBPGs are located in the points with large EOF values (absolute values) of at least one MGS.

35.0 km. The strike, dip, and rake angles of the hypothetical earthquake are 20°, 42°, and 121°, respectively, with a slip of 7.0 m. Figure 5a shows the initial sea surface deformation produced by this earthquake. It generates a tsunami that propagates towards the EMB (Figures 5b–5d). The rationale for this scenario is based on the study by Soloviev (1990) who informed that east Sicily is a major tsunamigenic zone in the EMB. Crete Island is along the direction of the short axis of the seismic fault (i.e., fault width), and thus, the tsunami energy is more concentrated towards this island. The tsunami waveforms obtained through forward tsunami simulation are called "synthetic waveforms" here which are shown in Figure 5e. The first tsunami peak arrives at the stations E02 and E01 at 59 min and 64 min after the earthquake, respectively (Figure 5e). The arrival times are 67 min and 69 min at the tide gauges Falasarna and Paleochora, respectively. The maximum tsunami amplitude of 19.3 cm is recorded at the tide gauge Falasarna. It has a comparatively smaller effect (<10.0 cm) on the tide gauge NOA-10, because it is located on the eastern side of the island (Figure 6).

The tsunami waveforms are forecasted using data assimilation approach and are updated continuously during the data assimilation process. The tsunami waveforms obtained by data assimilation are called "forecasted waveforms" here (Figure 6; red waveforms), which are compared with synthetic waveforms (Figure 6; black waveforms). The dashed line in Figure 6 indicates the end of data assimilation process. Therefore, the time interval between the end of the assimilation (i.e., dashed line in Figure 6) and the arrival of the tsunami at each tide gauge is the lead time for issuing tsunami warnings. At tide gauges NOA-4, NOA-10, and Soudhas, the lead time for tsunami warning is approximately 20 min. At Paleochora and Falasarna, the warning lead time is relatively shorter (i.e., approximately 10 min) due to the relatively short distance between the tide gauge and the OBPGs. Figure 6 indicates that our data assimilation approach forecasts the tsunami arrival times and first-peak amplitudes at all tide gauges well, with a warning leading time of 10–20 min. At NOA-04, NOA-10, and Soudhas, the amplitude of the first tsunami peak is accurately predicted by data assimilation. But at Falasarna, the forecasted amplitude (i.e., 11.0 cm) is smaller than the synthetic amplitude that is used for comparison (19.3 cm). The reason is that the tsunami arrives at Falasarna at an early time, even before it arrives at most OBPGs. We do not have much tsunami waveform data for assimilation. To the contrary, the stations on the middle or eastern part of Crete Island show a better match between the synthetic and forecasted waveforms. According to the performance quality index of Tsushima et al. (2012), the tsunami forecast accuracy (i.e., percentage of success) is calculated by: $\left[1-\frac{\sum_{i=1}^{N}(O_i-F_i)^2}{\sum_{i=1}^{N}(O_i)^2}\right]\times 100\%$. Here, O_i and F_i are the first-peak amplitude of the synthetic (used as observation) and forecasted tsunamis, respectively. Overall, the accuracy of data assimilation process for tsunami forecasting is 88.5% for a tsunami source in east Sicily. Though the maximum tsunami amplitude may come in later phase for far-field event at some stations (e.g., NOA-04 and Soudhas), which is not well predicted at a warning leading time of 10–20 min, we note that our tsunami early warning system is mainly aimed at forecasting the first wave).

3.3. Early Warning for Hypothetical Landslide Tsunamis

The tsunami generated by a landslide in Cyclades mainly affects the northern side of Crete Island (Figures 7a and 7d). We assume that a submarine landslide occurs at 37.0°N and 25.7°E. The region of the landslide is assumed to be a circle with a diameter of 1.5 km. The total amount of landslide volume is assumed to be 0.3 km^3, and the average thickness of the sliding mass is 170 m. The rationale for this scenario is based on

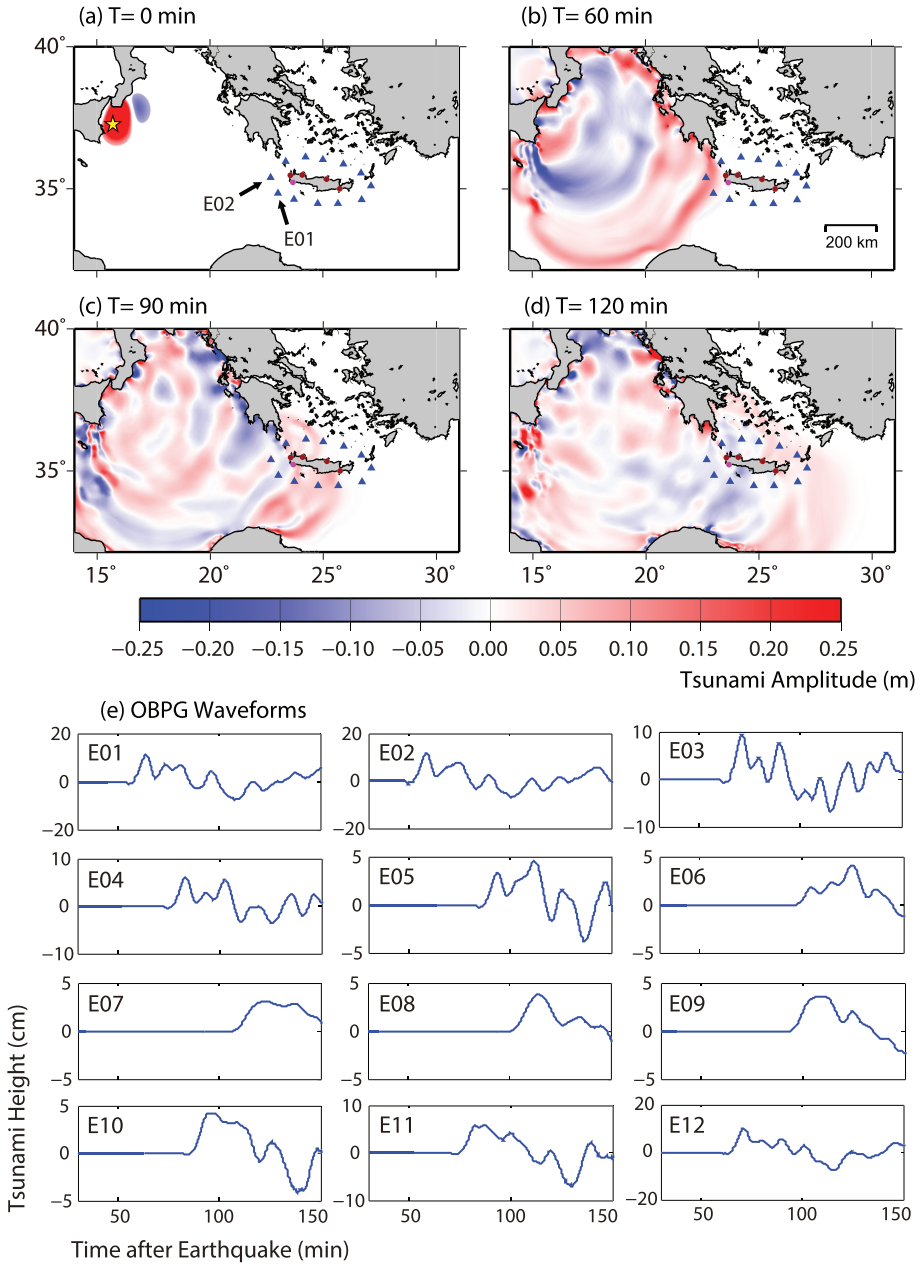

Figure 5. (a) Initial sea surface deformation due to the hypothetical earthquake in east Sicily. (b–d) Tsunami snapshots of the hypothetical seismogenic tsunami generated by an earthquake in east Sicily. (e) The synthetic waveforms at OBPGs from tsunami simulation that are used as input waveforms for data assimilation. The yellow star represents the epicenter of the earthquake.

the studies by Soloviev (1990) and Samaras et al. (2015) who showed that seismic activities in the Aegean Sea region have triggered tsunamigenic submarine landslides such as the events of the 1650 (M 6.3) and the 1968 (M 6.8).

The designed OBPGs on the north of Crete Island (E04–E07) received evident tsunami signals from this hypothetical landslide tsunami, but the tsunami heights of other OBPGs are less than 2.0 cm (Figure 7). Compared to the seismogenic tsunami, the landslide tsunami has a shorter wavelength, and there are more high-frequency components and dispersive characteristics in their waveforms. Hence, it is challenging to distinguish the arrival time of the first tsunami peak. Assuming the time of the landslide initiation as

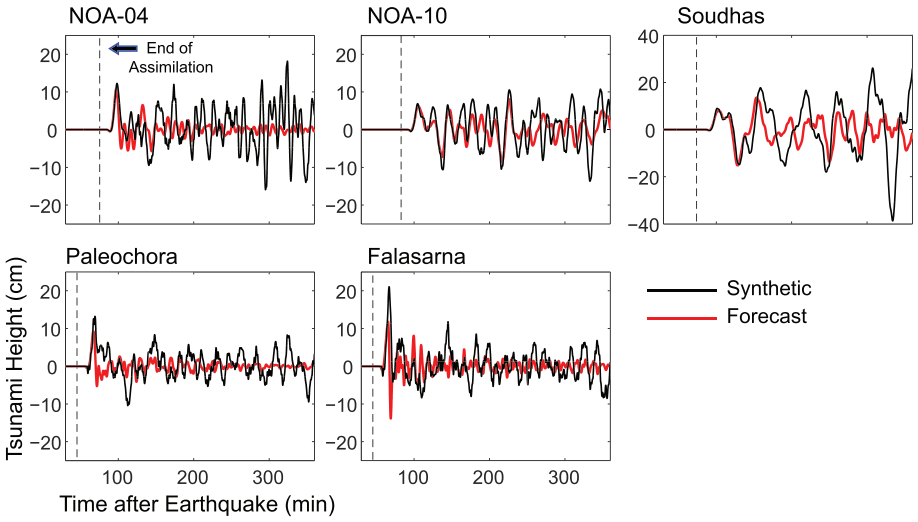

Figure 6. Comparison of the synthetic (black curves) and forecasted waveforms using data assimilation (red curves) at five tide gauges on Crete Island. The dashed vertical line indicates the end of the time window for tsunami data assimilation.

t = 0, the first tsunami peak arrives at t = 55 min at tide gauge NOA-10 with an amplitude of 3.0 cm (Figure 8). The maximum peak, which is 9.7 cm in amplitude, arrives later at NOA-10. At tide gauge Soudhas, the first peak arrives at t = 72 min with an amplitude of 3.3 cm. The tsunami heights are smaller (<3 cm) at tide gauges NOA-04 and Falasarna. Almost no tsunami signal can be seen at Paleochora.

The waveforms are forecasted at 10 min before the arrival of the tsunami's first peak by data assimilation approach (Figure 8). At both NOA-10 and Soudhas, the tsunami waveforms that are forecasted by data assimilation are consistent with the simulations (Figure 8), though the forecasted waveforms have less high-frequency components. At NOA-10, the tsunami arrival time and the first-peak amplitude are predicted accurately, but the maximum amplitude is not forecasted well. At Soudhas, the first-peak amplitude and the maximum amplitude are precisely forecasted. At NOA-04, our forecasted waveforms generally match with the simulation, but at Falasarna, it fails to predict the tsunami waveforms with a very small amplitude (i.e., <3 cm). Overall, considering the waveforms at tide gauges except for Paleochora, the forecast accuracy of our data assimilation approach for a hypothetical landslide tsunami is 87.3%.

Because the source size of landslide tsunamis is smaller than the seismogenic tsunamis, we make additional tests for landslide tsunamis and present them in the supporting information. They are the effects of noise in the OBPG waveforms (Supporting Information S2) and of station interval and the characteristic distance of data assimilation (Supporting Information S3) on the forecast. In our synthetic experiments presented above, we assumed that OBPG waveforms are noise-free, because OBPG is capable of detecting tsunamis of less than 1 cm (Kubota et al., 2020; Wang, Satake, et al., 2019), indicating that the associated noise level is relatively low. However, OBPG records can be affected by several natural interferences, particularly for landslide tsunamis because of the short period. In our Supporting Information S2, we conduct additional experiments by incorporating noise into the OBPG waveforms. We also examine the effect of shorter characteristic distance (5 km) than used in our data assimilation (20 km). The characteristic distance is the size of Gaussian-shape source for GFTDA (Figure 3b; Wang, Maeda, et al., 2019). Because the forecast accuracy is affected by both the characteristic distance and the station interval, we also change the station interval from 100 km to 25 km in the additional experiments (Supporting Information S3).

3.4. Early Warning for the May 2020 Off the Crete Tsunami

Besides hypothetical experiments, we also retrospectively use the tsunami generated by the 2 May 2020 earthquake (Mw 6.6) offshore Crete Island as a test case. The tsunami was recorded by the tide gauge NOA-04 on Crete Island (Figure 1). As there are no OBPGs located off the coast, we use the synthetic waveforms as the input for data assimilation. To compute the synthetic waveforms at OBPGs, we invert the tsunami data recorded at NOA-04 and estimate the source model of the 2020 event. A single fault with a

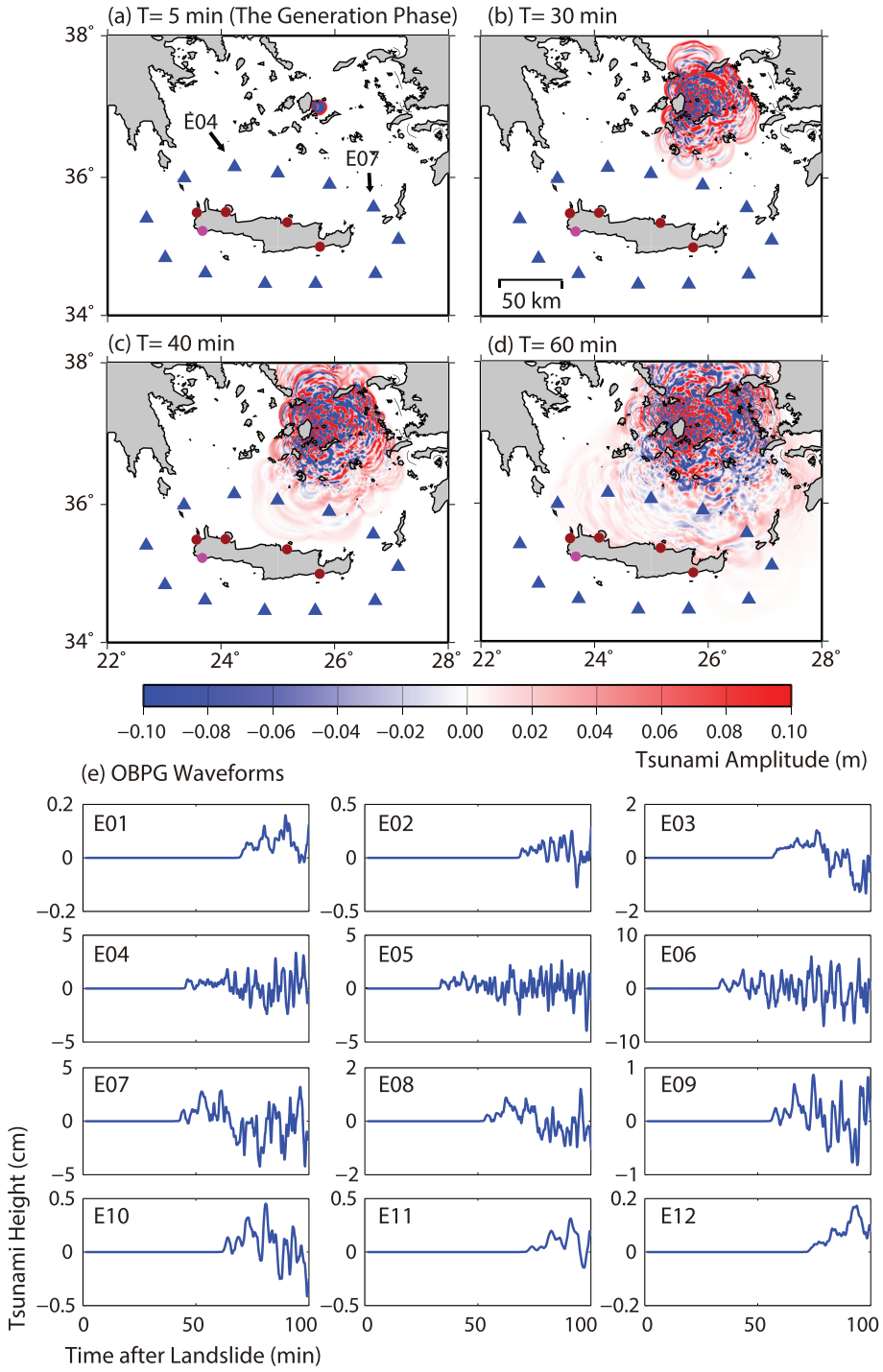

Figure 7. (a) Initial condition for modeling the tsunami generated by the landslide (i.e., the generation phase). (b–d) Tsunami snapshots of the hypothetical landslide tsunami generated in Cyclades in the Aegean Sea. (e) The synthetic waveforms at OBPGs from forward tsunami simulation that are used as input waveforms for data assimilation.

dimension of 20.0 km × 12.0 km and a slip of 1.5 m is used as the source of the tsunami. The epicenter is at 34.205°N, 25.712°E, and the top depth of the fault is 11.5 km based on the USGS. The centroid of this event is at 34.205°N, 25.712°E, with a depth of 12 km based on the Global Centroid-Moment-Tensor (CMT) Project. The strike, dip, and rake angles are 229°, 31°, and 46°, respectively, following the W-phase focal mechanism

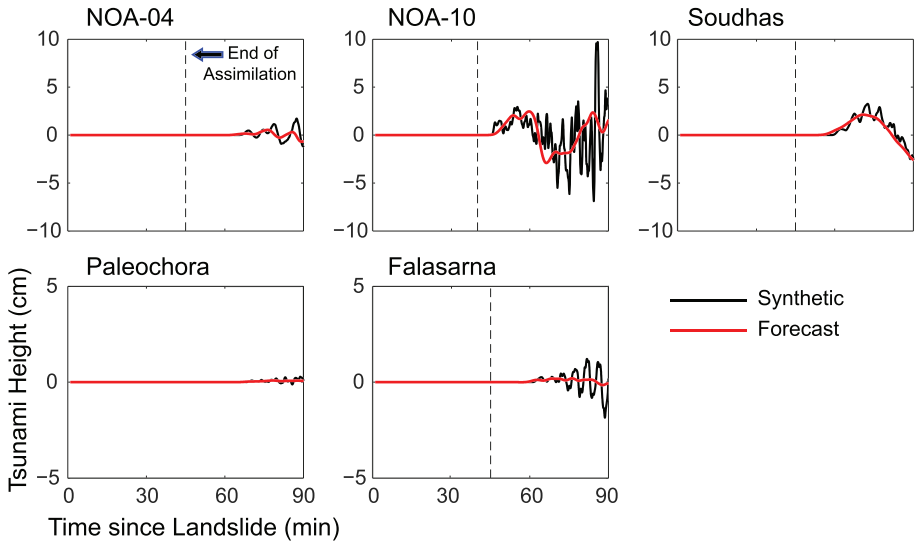

Figure 8. Comparison of the synthetic (black curves) and forecasted waveforms (red curves) at five tide gauges on Crete Island. The dashed vertical line indicates the end of the time window for tsunami data assimilation.

solution of the USGS for this event. Figure 9a shows the initial sea surface deformation caused by this earthquake.

Figures 9b–9d demonstrate the propagation of the tsunami and its wavefield. The tsunami arrives at E10 at around 5 min after the earthquake whereas it arrives at the southern coast of Crete Island at around 15 min after the earthquake. The tsunami waveforms at OBPGs obtained through numerical simulation are used for data assimilation (Figure 9e). In Figure 9e, we only plot the waveforms of the OBPGs where the tsunami arrives earlier than at tide gauge NOA-04. This means we apply only three OBPG records of E09, E10, and E11 for forecasting the tsunami at the coastal location NOA-04. The data assimilation process ends at 8 min after the earthquake, which is indicated by the dashed line in Figures 9e–9f.

The forecasted waveform using data assimilation is compared with the real observation and the synthetic waveform (Figure 9f). The synthetic waveform is consistent with the real observations for the first few waves, proving the validity of our source model and that the waveforms at OBPGs are reliable for tsunami data assimilation. Our assimilation predicts the tsunami arrival at tide gauge NOA-04 accurately, and it fairly forecasts the tsunami amplitude as well. For the first tsunami peak, the observed and forecasted amplitudes are 5.0 and 4.5 cm, which yields an accuracy of 99.0% calculated by the equation of quality index (Tsushima et al., 2012), and the observed and forecasted arrival times are 18 and 19 min, respectively. For the later phase, the forecasted waveform has a longer wavelength, but it fairly predicts the tsunami peaks at ~28 and 35 min. Because the assimilation process ends at 8 min, the tsunami warning lead time is ~10 min for the May 2020 event. Overall, the performance of the OBPG network in predicting the real May 2020 tsunami appears to be satisfactory despite its rather short arrival time of ~20 min. In this study, the size of the tsunami source is shorter than the distance between the two adjacent OBPGs (Figure 9a). In many cases of data assimilation efforts in the past, the size of a tsunami source spans at least several OBPGs. Therefore, it is believed that the result shown in Figure 9 for the May 2020 event is very important because it proves the success of the method even for small tsunamis.

4. Discussion

Unlike trans-Pacific tsunamis, tsunamis in the EMB propagate in a narrow and confined region (e.g., Heidarzadeh & Satake, 2013), and thus, tsunamis could propagate across the Mediterranean Sea in a short time (<1 h) and arrive at the coastal areas. The OBPGs designed in our study for the EMB are located in the narrow water body of the Mediterranean Sea and are aimed at detecting tsunamis and assimilating the observed data into early warning in a short time, mostly less than 30 min. For the data assimilation approach, we need sufficient observational data in order to provide accurate forecasts. In our test of the

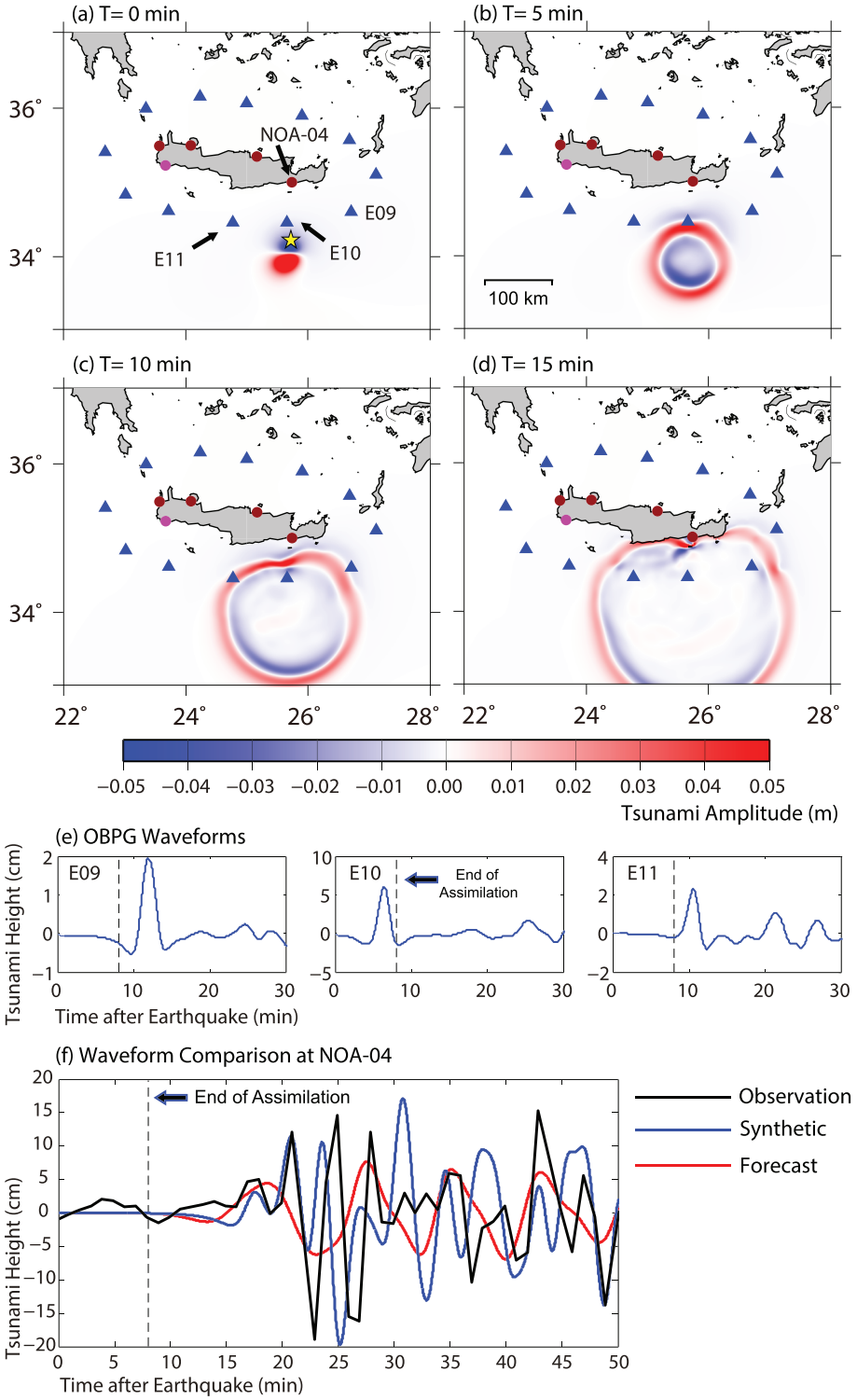

Figure 9. (a) Initial sea surface deformation due to the May 2020 off the Crete earthquake. (b–d) Tsunami snapshots generated by the May 2020 event. (e) The synthetic waveforms at OBPGs from forward tsunami simulation that are used as input waveforms for data assimilation. (f) Comparison of the observed (black curve), synthetic (blue curve) and forecasted waveforms (red curve) at tide gauges NOA-04. The dashed vertical line indicates the end of the time window for tsunami data assimilation. The yellow star represents the epicenter of the earthquake.

real tsunami of 2 May 2020, the earthquake occurred in the near-field at the distance of ~100 km from the coast, and the proposed OBPG station E10 is very close to the source region. In some cases, if the OBPG is located within the source regions, it cannot record the initial ocean surface displacement directly, because of the seismic waves and that fact that the ocean surface displacement is almost the same as the ocean bottom deformation (Saito et al., 2019; Saito & Tsushima, 2016; Tsushima et al., 2012). To overcome this problem, we could use the method developed by Tanioka (2018) to reproduce the tsunami height distribution correctly and make it available for tsunami data assimilation.

The early warning system that we proposed is applicable not only to seismogenic tsunamis, but also to landslide and volcanic tsunamis. This is extremely helpful in the EMB, due to its potential for a large variety of tsunamigenic sources (Soloviev, 1990). Traditional tsunami early warning systems based on seismic observations may fail to provide appropriate warnings for non-seismic tsunamis. Our approach is also useful in other regions worldwide where tsunamis are also generated by landslide or volcano eruption, like Indonesia and Japan (Heidarzadeh et al., 2020; Maeno & Imamura, 2011; Satake, 2007). For landslide tsunamis, the real practice of OBPGs for tsunami detection requires more caution. As discussed by Saito and Kubota (2020), the pressure induced by short-period waves on OBPGs deviates from hydrostatic relation if the wavelength of the sea-bottom deformation is not much greater than the sea depth. Last but not least, our designed early warning system aims to solely protect Crete Island, where high potential of tsunami damage exist. In case the warning system is aimed at protecting other regions such as Cyprus and west Turkey region, a new network of OBPG should be designed.

5. Conclusion

We proposed a potential early tsunami warning system based on tsunami data assimilation in the Eastern Mediterranean Basin (EMB). Twelve Offshore Bottom Pressure Gauge (OBPGs) are designed around Crete Island, and their locations are confirmed by performing Empirical Orthogonal Function (EOF) analysis. Our proposed warning system is able to forecast tsunami arrival time and first-peak amplitude in Crete Island accurately at 10–20 min before the tsunami arrival. The forecasting accuracy of the hypothetical seismogenic tsunami in east Sicily is 88.5%. It also works well for landslide tsunamis, though the high-frequency components of landslide-generated waves are not fully captured by the OBPG network. The forecasting accuracy of our data assimilation approach for the hypothetical landslide tsunami is 87.3%. Moreover, the retrospective study of the real tsunami event of 2 May 2020, generated by an Mw 6.6 earthquake off Crete Island, shows that our approach is able to predict the tsunami fairly well though it is a near-field tsunami with travel time of ~20 min. The observed and forecasted first-peak amplitudes are 5.0 and 4.5 cm, while the arrival times are 18 and 19 min, respectively. A warning lead time of ~10 min was obtained for the May 2020 event. We conclude that the deployment of OBPGs is helpful to tsunami early warning for Crete Island for both near-field and far-field tsunamis in the EMB. We recommend this method for other tsunamigenic zones in the EMB region such as the Aegean Sea and west Turkey and for beyond EMB such as Indonesia.

Data Availability Statement

The bathymetry data used in this work comes from the General Bathymetric Chart of the Ocean (GEBCO) (https://www.gebco.net/data_and_products/gebco_digital_atlas/). Sea level data are from the National Observatory of Athens (NOA) (http://www.noa.gr/index.php?lang=en) and the Intergovernmental Oceanographic Commission (IOC) (http://www.ioc-sealevelmonitoring.org/station.php?code=avon). We used the *JAGURS* tsunami simulation code (Baba et al., 2015; available at https://github.com/jagurs-admin/jagurs) and the TDAC data assimilation code (Maeda et al., 2015; available at https://github.com/takuto-maeda/tdac). The processed bathymetry data, tide gauge records, and station lists used in this paper are available in the public repository https://figshare.com/articles/dataset/Bathymetry_and_Station_List_for_Tsunamis_in_EMB/12780800.

Acknowledgments

This work is partly supported by the Royal Society, UK, grant number CHL \R1\180173 (M. H.), and JSPS KAKENHI 16H01838 (K. S.) and 19J20293 (Y. W.). Y. W. thanks Dr. Zhouqiao Zhao of Peking University for his help with job script.

References

Baba, T., Takahashi, N., Kaneda, Y., Ando, K., Matsuoka, D., & Kato, T. (2015). Parallel implementation of dispersive tsunami wave modeling with a nesting algorithm for the 2011 Tohoku Tsunami. *Pure and Applied Geophysics*, *172*, 3455–3472. https://doi.org/10.1007/s00024-015-1049-2

Cohen, K., Siegel, S., & McLaughlin, T. (2003). *Sensor placement based on proper orthogonal decomposition modeling of a cylinder wake* (Vol. 4259, pp. 2003–4259). Paper presented at 33rd AIAA Fluid Dynamics Conference, AIAA, Orlando, FL. https://doi.org/10.2514/6.2003-4259

Dogan, G. G., Annunziato, A., Papadopoulos, G. A., Guler, H. G., Yalciner, A. C., Cakir, T. E., et al. (2019). The 20th July 2017 Bodrum-Kos tsunami field survey. *Pure and Applied Geophysics*, *176*, 2925–2949. https://doi.org/10.1007/s00024-019-02151-1

Dominey-Howes, D. T. M., Papadopoulos, G. A., & Dawson, A. G. (2000). Geological and historical investigation of the 1650 Mt. Columbo (Thera Island) eruption and tsunami, Aegean Sea, Greece. *Natural Hazards*, *21*, 83–96. https://doi.org/10.1023/A:1008178100633

Furumura, T., Maeda, T., & Oba, A. (2018). Early forecast of long-period ground motions via data assimilation of observed ground motions and wave propagation simulations. *Geophysical Research Letters*, *46*, 138–147. https://doi.org/10.1029/2018GL081163

Gusman, A. R., Mulia, I. E., Satake, K., Watada, S., Heidarzadeh, M., & Sheehan, A. F. (2016). Estimate of tsunami source using optimized unit sources and including dispersion effects during tsunami propagation: The 2012 Haida Gwaii earthquake. *Geophysical Research Letters*, *43*, 9819–9828. https://doi.org/10.1002/2016GL070140

Heidarzadeh, M., & Gusman, A. R. (2018). Application of dense offshore tsunami observations from Ocean Bottom Pressure Gauges (OBPGs) for tsunami research and early warnings. In *Geological disaster monitoring based on sensor networks* (pp. 7–22). Singapore: Springer Natural Hazards. https://doi.org/10.1007/978-981-13-0992-2_2

Heidarzadeh, M., Ishibe, T., Sandanbata, O., Muhari, A., & Wijanarto, A. B. (2020). Numerical modeling of the subaerial landslide source of the 22 December 2018 Anak Krakatoa volcanic tsunami, Indonesia. *Ocean Engineering*, *195*, 106733. https://doi.org/10.1016/j.oceaneng.2019.106733

Heidarzadeh, M., Krastel, S., & Yalciner, A. C. (2014). The state-of-the-art numerical tools for modeling landslide tsunamis: A short review. In *Submarine mass movements and their consequences* (Chap. 43, pp. 483–495). Springer: International publishing. https://doi.org/10.1007/978-3-319-00972-8_43

Heidarzadeh, M., Necmioglu, O., Ishibe, T., & Yalciner, A. C. (2017). Bodrum-Kos (Turkey-Greece) Mw 6.6 earthquake and tsunami of 20 July 2017: A test for the Mediterranean tsunami warning system. *Geoscience Letters*, *4*, 31. https://doi.org/10.1186/s40562-017-0097-0

Heidarzadeh, M., & Satake, K. (2013). The 21 May 2003 tsunami in the Western Mediterranean Sea: Statistical and wavelet analyses. *Pure and Applied Geophysics*, *170*(9–10), 1449–1462. https://doi.org/10.1007/s00024-012-0509-1

Heidarzadeh, M., Wang, Y., Satake, K., & Mulia, I. E. (2019). Potential deployment of offshore bottom pressure gauges and adoption of data assimilation for tsunami warning system in the western Mediterranean Sea. *Geoscience Letters*, *6*, 19. https://doi.org/10.1186/s40562-019-0149-8

Kaneda, Y. (2010). The advanced ocean floor real time monitoring system for mega thrust earthquakes and tsunamis-application of DONET and DONET2 data to seismological research and disaster mitigation. OCEAN 2010. https://doi.org/10.1109/OCEANS.2010.5664309

Kawamata, K., Takaoka, K., Ban, K., Imamura, F., Yamaki, S., & Kobayashi, E. (2005). Model of tsunami generation by collapse of volcanic eruption: The 1741 Oshima-Oshima tsunami. In K. Satake (Ed.), *Tsunamis: Case studies and recent developments* (pp. 79–96). New York: Springer. https://doi.org/10.1007/1-4020-3331-1_5

Kubota, T., Saito, T., & Suzuki, W. (2020). Millimeter-scale tsunami detected by a wide and dense observation array in the deep ocean: Fault modeling of an Mw 6.0 Interplate Earthquake off Sanriku, NE Japan. *Geophysical Research Letters*, *47*, e2019GL085842. https://doi.org/10.1029/2019GL085842

Liu, M., Lin, J., Wang, Y., Sun, Y., Zheng, B., Shao, J., et al. (2018). Spatiotemporal variability of NO_2 and $PM_{2.5}$ over Eastern China: Observational and model analyses with a novel statistical method. *Atmospheric Chemistry and Physics*, *18*, 12933–12952. https://doi.org/10.5194/acp-18-12933-2018

Lorentz, E. N. (1956). Empirical orthogonal functions and statistical weather prediction. In statistical forecasting report: Scientific report no. 1 (pp. 49). Cambridge: Massachusetts Institute of Technology, Department of Meteorology.

Maeda, T., Obara, K., Shinohara, M., Kanazawa, T., & Uehira, K. (2015). Successive estimation of a tsunami wavefield without earthquake source data: A data assimilation approach toward real-time tsunami forecasting. *Geophysical Research Letters*, *42*, 7923–7932. https://doi.org/10.1002/2015GL065588

Maeno, F., & Imamura, F. (2011). Tsunami generation by a rapid entrance of pyroclastic flow into the sea during the 1883 Krakatau eruption, Indonesia. *Journal of Geophysical Research*, *116*, B09205. https://doi.org/10.1029/2011JB008253

Mulia, I. E., Gusman, A. R., & Satake, K. (2017). Optimal design for placements of tsunami observing systems to accurately characterize the inducing earthquake. *Geophysical Research Letters*, *44*, 12,106–12,115. https://doi.org/10.1002/2017GL075791

Mulia, I. E., Gusman, A. R., Williamson, A. L., & Satake, K. (2019). An optimized array configuration of tsunami observation network off Southern Java, Indonesia. *Journal of Geophysical Research: Solid Earth*, *124*, 9622–9637. https://doi.org/10.1029/2019JB017600

Navarrete, P., Cienfuegos, R., Satake, K., Wang, Y., Urrutia, A., Benavente, R., et al. (2020). Sea surface network optimization for tsunami forecasting in the near field: Application to the 2015 Illapel earthquake. *Geophysical Journal International*, *221*, 1640–1650. https://doi.org/10.1093/gji/ggaa098

Okada, Y. (1985). Surface deformation due to shear and tensile faults in a half-space. *Bulletin of the Seismological Society of America*, *75*(4), 1135–1154. https://doi.org/10.1016/0148-9062(86)90674-1

Okal, E. A., Synolakis, C. E., Uslu, B., Kalligeris, N., & Voukouvalas, E. (2009). The 1956 earthquake and tsunami in Amorgos, Greece. *Geophysical Journal International*, *178*, 1533–1554. https://doi.org/10.1111/j.1365-246X.2009.04237.x

Papadopoulos, G. A., Daskalaki, E., & Fokaefs, A. (2007). Tsunamis generated by coastal and submarine landslides in the Mediterranean Sea, Submarine mass movements and their consequences. In V. Lykousis, D. Sakellariou, & J. Locat (Eds.), *Advances in natural and technological hazards research* (Vol. 27, pp. 415–422). Dordrecht: Springer. https://doi.org/10.1007/978-1-4020-6512-5_43

Papadopoulos, G. A., Daskalaki, E., Fokaefs, A., & Giraleas, N. (2007). Tsunami hazards in the Eastern Mediterranean: Strong earthquakes and tsunamis in the East Hellenic Arc and Trench system. *Natural Hazards and Earth System*, *7*(1), 57–64. https://doi.org/10.5194/nhess-7-57-2007

Papadopoulos, G. A., Lekkas, E., Katsetsiadou, K. N., Rovythakis, E., & Yahav, A. (2020). Tsunami alert efficiency in the Eastern Mediterranean Sea: The 2 May 2020 earthquake (Mw6.6) and near-field tsunami south of Crete (Greece). *GeoHazards*, *1*(1), 44–60. https://doi.org/10.3390/geohazards1010005

Ren, Z., Wang, Y., Wang, P., Hou, J., Gao, Y., & Zhao, L. (2020). Numerical study of the triggering mechanism of the 2018 Anak Krakatau Tsunami: Eruption or collapsed landslide? *Natural Hazards*, *102*, 1–13. https://doi.org/10.1007/s11069-020-03907-y

Saito, T., Baba, T., Inazu, D., Takemura, S., & Fukuyama, E. (2019). Synthesizing sea surface height change including seismic waves and tsunami using a dynamic rupture scenario of anticipated Nankai trough earthquakes. *Tectonophysics*, *769*, 228166. https://doi.org/10.1016/j.tecto.2019.228166

Saito, T., & Kubota, T. (2020). Tsunami modeling for the deep sea and inside focal areas. *Annual Review of Earth and Planetary Sciences*, *48*, 121–145. https://doi.org/10.1146/annurev-earth-071719-054845

Saito, T., & Tsushima, H. (2016). Synthesizing ocean bottom pressure records including seismic wave and tsunami contributions: Toward realistic tests of monitoring systems. *Journal of Geophysical Research: Solid Earth*, *121*, 8175–8195. https://doi.org/10.1002/2016JB013195

Samaras, A. G., Karambas, T. V., & Archetti, R. (2015). Simulation of tsunami generation, propagation and coastal inundation in the Eastern Mediterranean. *Ocean Science*, *11*, 643–655. https://doi.org/10.5194/os-11-643-2015

Satake, K. (1995). Linear and nonlinear computations of the 1992 Nicaragua earthquake tsunami. *Pure and Applied Geophysics*, *144*(3–4), 455–470. https://doi.org/10.1007/BF00874378

Satake, K. (2007). Volcanic origin of the 1741 Oshima-Oshima tsunami in the Japan Sea. *Earth, Planets and Space*, *59*(5), 381–390. https://doi.org/10.1186/BF03352698

Satake, K. (2012). Tsunamis generated by submarine landslides. In *Submarine mass movements and their consequences* (pp. 475–484). Dordrecht: Springer. https://doi.org/10.1007/978-94-007-2162-3_42

Satake, K. (2014). Advances in earthquake and tsunami sciences and disaster risk reduction since the 2004 Indian ocean tsunami. *Geoscience Letters*, *1*, 15. https://doi.org/10.1186/s40562-014-0015-7

Satake, K. (2015). Tsunamis. In G. Schubert (Ed.), *Treatise on Geophysics* (2nd ed., Vol. 4, pp. 477–504). Oxford: Elsevier. https://doi.org/10.1016/B978-0-444-53802-4.00086-5

Satake, K., & Heidarzadeh, M. (2017). A review of source models of the 2015 Illapel, Chile earthquake and insights from tsunami data. *Pure and Applied Geophysics*, *174*(1), 1–9. https://doi.org/10.1007/s00024-016-1450-5

Shaw, B., Ambraseys, N. N., England, P. C., Floyd, M. A., Gorman, G. J., Higham, T. F. G., et al. (2008). Eastern Mediterranean tectonics and tsunami hazard inferred from the AD 365 earthquake. *Nature Geoscience*, *1*(4), 268–276. https://doi.org/10.1038/ngeo151

Soloviev, S. L. (1990). Tsunamigenic zones in the Mediterranean Sea. *Natural Hazards*, *3*(2), 183–202. https://doi.org/10.1007/BF00140432

Tanioka, Y. (2018). Tsunami simulation method assimilating ocean bottom pressure data near a tsunami source region. *Pure and Applied Geophysics*, *175*, 721–729. https://doi.org/10.1007/s00024-017-1697-5

The United States Geological Survey (USGS) (2020). Information on M 6.6-89km S of Ierapetra, Greece. https://earthquake.usgs.gov/earthquakes/eventpage/us700098qd/executive. Accessed 2 May 2020.

Tsushima, H., Hino, R., Tanioka, Y., Imamura, F., & Fujimoto, H. (2012). Tsunami waveform inversion incorporating permanent seafloor deformation and its application to tsunami forecasting. *Journal of Geophysical Research*, *117*, B03311. https://doi.org/10.1029/2011JB008877

Wang, Y., Maeda, T., Satake, K., Heidarzadeh, M., Su, H., Sheehan, A. F., & Gusman, A. R. (2019). Tsunami data assimilation without a dense observation network. *Geophysical Research Letters*, *46*, 2045–2053. https://doi.org/10.1029/2018GL080930

Wang, Y., Satake, K., Maeda, T., & Gusman, A. R. (2017). Green's Function-based Tsunami Data Assimilation (GFTDA): A fast data assimilation approach toward tsunami early warning. *Geophysical Research Letters*, *44*, 10,282–10,289. https://doi.org/10.1002/2017GL075307

Wang, Y., Satake, K., Maeda, T., & Gusman, A. R. (2018). Data assimilation with dispersive tsunami model: A test for the Nankai Trough. *Earth, Planets and Space*, *70*, 131. https://doi.org/10.1186/s40623-018-0905-6

Wang, Y., Satake, K., Sandanbata, O., Maeda, T., & Su, H. (2019). Tsunami data assimilation of cabled ocean bottom pressure records for the 2015 Torishima volcanic tsunami earthquake. *Journal of Geophysical Research: Solid Earth*, *124*, 10,413–10,422. https://doi.org/10.1029/2019JB018056

Weatherall, P., Marks, K. M., Jakobsson, M., Schmitt, T., Tani, S., Arndt, J. E., et al. (2015). A new digital bathymetric model of the world's oceans. *Earth and Space Science*, *2*, 331–345. https://doi.org/10.1002/2015EA000107

Yalciner, A. C., Annunziato, A., Papadopoulos, G., Dogan, G. G., Guler, H. G., Cakir, T. E., et al. (2017). *The 20th July 2017 (22:31 UTC) Bodrum/Kos earthquake and tsunami: Post tsunami field survey report*. Retrieved from http://users.metu.edu.tr/yalciner/july-21–2017-tsunami-report/Report-FieldSurvey-of-July-20-2017-Bodrum-Kos-Tsunami.pdf (Accessed 30 March 2018)

Yalciner, A. C., Zaytsev, A., Aytore, B., Insel, I., Heidarzadeh, M., Kian, R., & Imamura, F. (2014). A possible submarine landslide and associated tsunami at the Northwest Nile Delta, Mediterranean Sea. *Oceanography*, *27*(2), 68–75. https://doi.org/10.5670/oceanog.2014.41